Mechanical Systems and Signal Processing 188 (2023) 110032

Contents lists available at ScienceDirect

Mechanical Systems and Signal Processing

journal homepage: www.elsevier.com/locate/ymssp

Design and optimization of a quadrupedal dynamic disturbance force measurement platform using strain gauges

Chengbo Zhou [a,b], Mingyi Xia [a,*], Zhenbang Xu [a,b,*]

[a] Changchun Institute of Optics, Fine Mechanics and Physics, Chinese Academy of Science, Jilin, Changchun 130033, China
[b] Center of Materials Science and Optoelectronics Engineering, University of Chinese Academy of Sciences, Beijing 100049, China

A R T I C L E I N F O

Communicated by Yaguo Lei

Keywords:
Vibration
Force measurement platform
Response surface methodology
D optimization

A B S T R A C T

A novel quadrupedal dynamic disturbance force measurement platform is described for the measurement of the disturbance forces of low-frequency sources in large optical facilities on the ground. The support of four strain monopodia makes the measuring platform more rigid. The optimal structural parameters of the strain monopodia are obtained adopting response surface methodology, which allows the sensitivity and stiffness of the platform to be balanced. D optimization is adopted to obtain a more accurate calibration matrix from the redundant outputs and thus improve the measurement accuracy of the platform. Model simulation results show that the load capacity of the measurement platform is more than 1000 kg. Using the results of theoretical analysis, a prototype system was fabricated and tested. The experimental results show that the fundamental frequency of the platform is 749.5 Hz, the dynamic relative error is less than 5.6 % in the frequency range of 3–300 Hz, and the static relative error is less than 5 %. The linearity of the generalized force is within 1.5 %FS, and the repeatability is within 1.1 %FS.

1. Introduction

Performance requirements for the resolution, stability and pointing accuracy of highly stable spacecraft such as large space telescopes have increased as the exploration of deep space continues to advance. In the case of the Chinese Space Station Telescope, a spectroscopic survey is capable of delivering stellar radial velocities to a precision of 2–4 km s^{-1} for AFGKM types of stars (according to the Harvard classification, and M−type stars are lower temperature stars) at a signal-to-noise ratio of 100 [1] and the aim is to perform the high-spatial-resolution (∼0.15″) imaging of targets that cover a large area of the sky (∼17,500 deg^2) and wide wavelength range [2]. However, even small vibrations can affect the accuracy of such sophisticated devices. In light of this concern, it is necessary to evaluate the effects of forces generated by vibration sources on the ground. In addition, the spacecraft carries low-frequency vibration sources, such as shutters and swing mirrors. Simulation has revealed that vibrations below 20 Hz generate greater force, and there is thus a need for good low-frequency measurement performance of the equipment used in the measurement of disturbance forces [3]. Moreover, the moving parts on spacecraft have become larger; e.g., the mass of a control moment gyroscope onboard the Chinese Space Station Telescope is 90 kg, and six control moment gyroscopes are usually used in a group for large space telescopes [4]. After the installation equipment is added, the measurement device will generally need to support loads greater than 1 ton in a micro-vibration ground test [5]. Additionally, with a diameter of nearly 2 m per functional module, a larger mounting plane is required for fixing and measuring. Given the above, there is a need for a force measurement platform having greater size and load capacity and, in particular,

* Corresponding authors.
E-mail addresses: xiamingyi@ciomp.ac.cn (M. Xia), xuzhenbang@ciomp.ac.cn (Z. Xu).

https://doi.org/10.1016/j.ymssp.2022.110032
Received 4 April 2022; Received in revised form 30 June 2022; Accepted 10 December 2022
Available online 19 December 2022
0888-3270/

having better performance in low-frequency measurements. Existing measurement systems hardly meet these requirements.

There are basically-two types of common force measuring devices in terms of the sensing elements: piezoelectric-ceramic-based measurement devices [4,6–11] and strain-gauge-based measurement devices [12–27]. Although piezoelectric sensors respond quickly, bear heavy loads and perform well in making dynamic measurements [4,6,9], their poor static and low-frequency dynamic measurement performance [11] make them inadequate for the above tasks. Strain-gauge-based sensors have good properties that are lacking for piezoelectric devices. Liu [13], for example, proposed a new six-component force sensor with four identical *T*-shaped bars as force sensing members, and this strain-gauge-based sensor achieved good results in terms isotropy and sensitivity during static measurement. However, the results presented in the cited article are based purely on a theoretical study. Jacq [16] designed and fabricated a force/torque sensor having six degrees of freedom (DOFs) for wrist rehabilitation, and Sun [20] developed a six-axis force/torque sensor equipped on the space robot that senses the three orthogonal forces and torques simultaneously. All these sensors perform well in terms of nonlinearity, repeatability, stability, hysteresis, sensitivity and accuracy but they are not used for dynamic measurements. Wu et al. [18] tested a multi-axis force strain-gauge-based sensor applied to a humanoid robot foot and verified that the sensor has good dynamic testing performance even at the low frequencies of walking. The strain-gauge-based sensor is selected in the present study as the sensing element for the measurement platform owing to its good static and low-frequency dynamic measurement performance. However, the previous measurement platforms based on strain gauge technology fail to measure dynamic disturbance forces in large mass and volume equipment, particularly in the low frequency band, considering the dynamic performance of the platform.

The accuracy and stiffness of the measuring platform is determined not only by the choice of the different sensing elements mentioned above but also by the structures of the platform. Hitherto, two typical types of force measuring device have been extensively studied, namely cross-shape devices [4,6,9,31,32] and Stewart platform devices [28–30]. However, the introduction of coupling is unavoidable for measurements of large-mass vibration sources owing to the loose structure of the Stewart platform, which reduces the stiffness of the structure, and Stewart platform devices have large size and high installation requirements. The cross-shape devices do not have these disadvantages. Li [32] proposed a six-DOF force/moment sensor for heavy load measurement that adopted a four-point redundant parallel configuration and studied the structure of the sensor, the arrangement of the force sensing elements and a load sharing method. The designed sensor greatly reduces the size, improves the measurement accuracy and load capacity, and has good high frequency band dynamic characteristics. The downside to this measurement device is that it is more suited to mounting on arm joints, and it is not possible to mount a large vibration source on the device. Xia [4] manufactured a piezoelectric platform capable of measuring the disturbance force of large moving devices on the ground and improved the measurement platform stiffness using an eight-point support (involving eight piezoelectric sensors). However, redundant measurements inevitably introduce systematic errors, which reduce the accuracy of the measurement. Therefore, the cross-shaped (four-point) structure mentioned above is usually chosen to improve the rigidity and accuracy of the measurement platform.

On the above basis, this paper proposes a strain-gauge-based quadrupedal low-frequency disturbance force measurement platform. To improve the sensitivity, stiffness and measurement accuracy, we conducted systematic work on the structural design, structural optimization and calibration algorithm. Section 2 describes the basic structure of the described platform and finds that the sensitivity and stiffness of the platform are a pair of contradictory indicators by means of finite element analysis (FEA). Section 3 optimizes the structural parameters of the strain monopodia of the platform adopting response surface methodology, such that the stiffness and sensitivity of the platform are obtained optimally. Section 4 systematically describes the working principle of the measurement

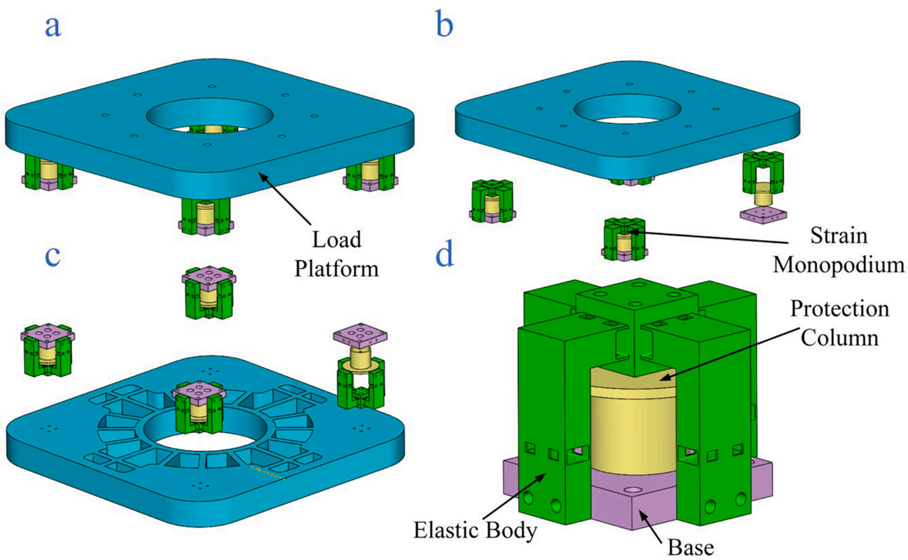

Fig. 1. Basic model of the measurement system: (a) assembly model of the platform; (b) explosion model of the platform viewed from the top; (c) explosion model of the platform viewed from the bottom; (d) assembly model of the strain monopodium.

platform and improves the measurement accuracy through D optimization. Section 5 describes experiments conducted for the evaluation of the static mechanical characteristics and dynamic mechanical characteristics of the platform, verifies that the proposed platform has better low frequency measurement accuracy than the piezoelectric platform and confirms the validity of the D optimization. Conclusions are drawn in Section 6.

2. Structural design

2.1. Basic structure

The structure of the measurement platform includes a load platform and four strain monopodia as shown in Fig. 1. A strain monopodium comprises a protection column, base and elastic body. The elastic body includes horizontal (position) beams (1), vertical beams (2), connecting blocks (3), upper block (4) and lower blocks (5) as shown in Fig. 2.

The proposed platform is mounted on a vibration isolator via the base to reduce the unwanted effect of vibrations on the measurement, and the vibration source is fixed to the load platform. In this case, the vibration of the source can be measured by the platform. The proposed measurement platform differs from traditional strain-gauge-based sensors [20,22], which have only one elastic body for detecting the six-DOF forces/moments. One strain monopodium of the measurement platform in this paper is equivalent to a three-DOF force sensor used to detect the forces F_x, F_y and F_z. Thus, 12 forces from four strain monopodia can be used to solve for the six-DOF forces/moments of the vibration source (not all 12 output signals are used, the remaining output channels can be used as a backup and to improve measurement accuracy with D optimization). This improves the rigidity of the measurement platform while taking advantage of the high sensitivity and good low-frequency characteristics of the strain gauges.

The Cartesian coordinate system is shown in Fig. 2. The x-axis vertical beams which are located on the x-axis and in the vertical position are used to detect F_x, the y-axis vertical beams are used to detect F_y, and the horizontal beams are used to detect F_z. The x-axis vertical beams, y-axis vertical beams and horizontal beams are orthogonal to each other, which effectively reduces the coupling error and improves the sensitivity.

The strain monopodium has a protective function that prevents the elastic body from being destroyed in the case of overloading. The gaps between the protection column and elastic body are accurately obtained using the finite element method (FEM) and are determined by the overload capacity of the strain monopodium.

2.2. FEA of the structure

An FEA was performed on the designed strain monopodium, the model was meshed (tet10 elements which can adapt to complex geometries were mainly used, the number of elements in the model is 60555, the number of nodes is 14351) and the strain was calculated with MSC/Nastran software. Fig. 3 shows that the x-axis vertical beams have appreciable strain near the strain gauges when the strain monopodium is subjected to an x-directional force, whereas the y-axis vertical and horizontal beams have less strain near the strain gauges. There are similar situations when the strain monopodium is subjected to y-directional and z-directional forces. It is inferred that the strain monopodium has less dimensional coupling and the measurement accuracy will be improved.

In addition, it is found that changing the structural parameters of the elastic body, as shown in Fig. 4, alters the sensitivity (characterized by the strain under a force of 1 N) and stiffness (characterized by the fundamental frequency) of the strain monopodium. Importantly, sensitivity and stiffness are a contradictory pair of indicators; i.e., an increase in sensitivity reduces the stiffness. It is thus necessary to find the optimal structural parameters of the elastic body so that the sensitivity and stiffness of the platform are optimized

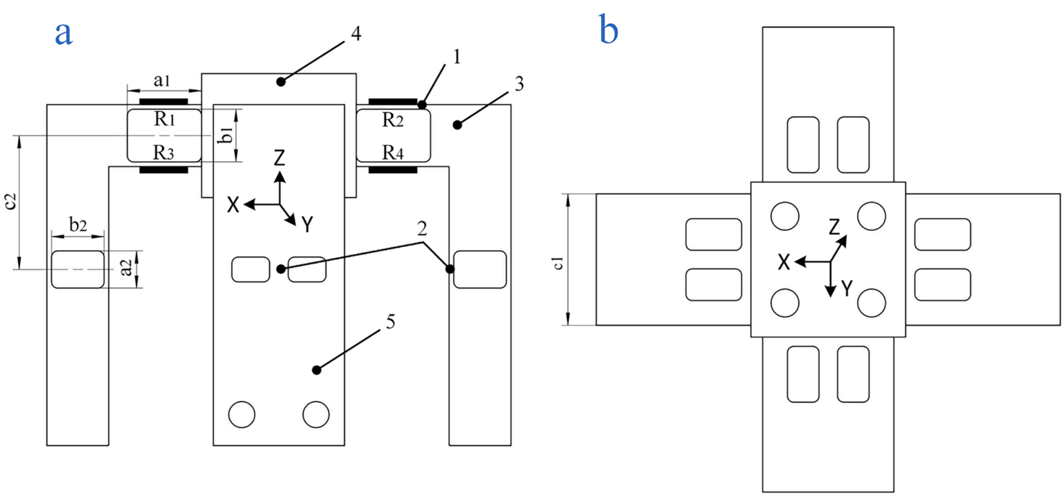

Fig. 2. Elastic body: (a) front view; (b) top view.

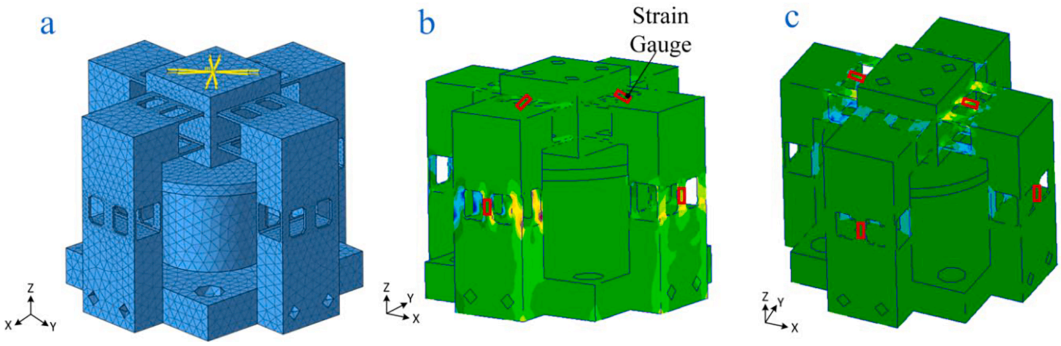

Fig. 3. FEA of the strain monopodium: (a) FEM mesh; (b) elastic strain (Z axis) under $F_x = 1$ N; (c) elastic strain (X axis) under $F_z = 1$ N.

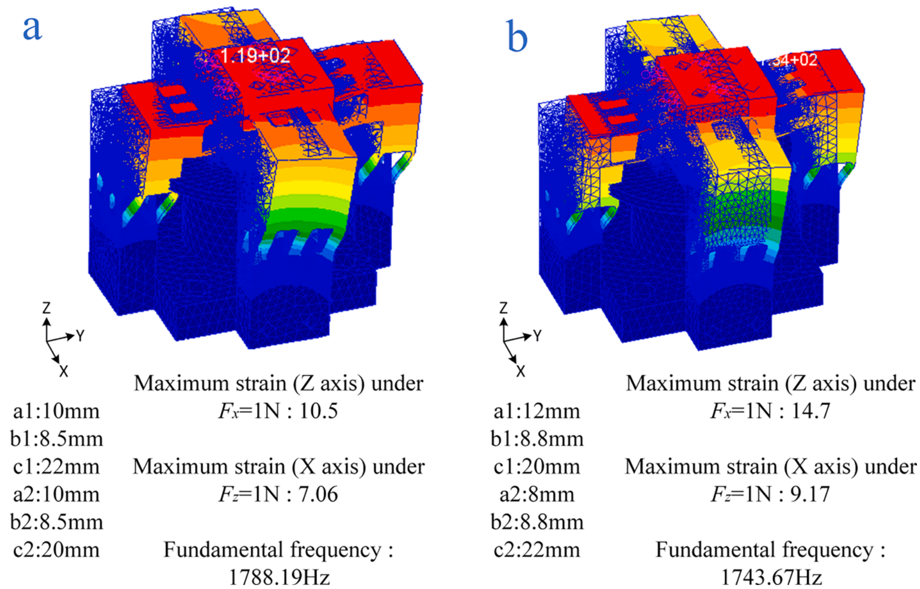

Fig. 4. FEA of the strain monopodium with different parameters.

simultaneously and the platform can meet the measurement requirements of the optical facilities. In making the optimization more convenient, and because the dimensions of the load platform remain the same and the mounting position of the strain monopodium is invariant, we use the stiffness of the strain monopodium to characterize the stiffness of the measurement platform.

3. Structural optimization

3.1. Design conditions

The required load capacity of the measurement platform is 500 kg. Owing to the good linearity and isotropy of the elastic body at the yield limit, we choose aluminum alloy for the manufacture of the elastomer. The material of the elastic body is 7075-T6 aluminum alloy, which has an elastic modulus $E = 7.2 \times 10^{10}\text{N/m}^2$, Poisson's ratio $\nu = 0.33$, density $\rho = 2.8 \times 10^3$ kg/m^3, yield strength $\sigma_s = 460$ MPa and safety factor $S = 1.2$.

The full-bridge strain gauges are used to amplify the small strain. The parameters of the strain gauge are given in Table 1.

Six parameter variables that affect the sensitivity and stiffness of the strain monopodium are set (Fig. 2): the length a_1 and width b_1 of the hole in the horizontal beam, width c_1 of the connecting block, length a_2 and width b_2 of the hole in the vertical beam, and length

Table 1
Parameters of the strain gauge.

Parameters	Gauge dimensions	Substrate dimensions	Gauge resistance	Sensitivity factor
Value	1 mm × 2 mm	3 mm × 5 mm	120 ± 0.1 Ω	2.08 ± 1 %

c_2 between the center line of the hole in the vertical beam and the center line of the upper block.

3.2. Optimization method

To obtain the best performance of the strain monopodium, the structural parameters of the elastic body are optimized in MSC/Patran software. The specific optimization process is presented in Fig. 5. There are numerous approaches to designing experiments [33–35], such as the central composite design and Box–Behnken design (BBD). The BBD, which is suitable for mechanical size optimization, was chosen because it avoids extreme points [36]. The range of values of the structural parameters to be optimized is given in Table 2.

Because the structure of the elastic body is symmetrical, the elastic deformation is similar when the body is subjected to x-directional and y-directional forces. Therefore, for the convenience of simulation, only the maximum strain near the strain gauge when the elastic body is subjected to x-directional and z-directional forces is used as the objective function (E_x-max, E_z-max). In addition, the fundamental frequency of the strain monopodium is used as the objective function (Fq). On the basis of the BBD experimental design, 54 sets of experiments were designed using the Design-Expert software. Each group of experiments is modeled and analyzed using the FEM, and the objective function values are recorded.

3.3. Optimized result

The expressions for E_x-max, E_z-max and Fq in the objective function can be obtained using response surface methodology:

$$\begin{aligned} Ex - \max = {} & 113.68 + 0.34a1 - 7.17b1 - 0.54c1 + 3.68a2 - 22.70b2 - 0.95c2 \\ & -0.34a2b2 + 0.60b1b2 + 0.16b1c2 - 0.04a2^2 + 1.43b2^2 \end{aligned} \tag{1}$$

$$Ez - \max = 66.23 - 1.96a1 - 14.78b1 - 0.19c1 + 0.30a1b1 + 0.89b1^2 \tag{2}$$

$$\begin{aligned} Fq = {} & -7134.71 + 34.30a1 + 861.55b1 + 130.95c1 + 51.19a2 + 1329.11b2 \\ & +46.96c2 - 16.22a1b1 + 1.40a1c1 + 0.95a1a2 + 10.07a1b2 - 0.61a1c2 \\ & +4.95a2b1 + 0.08a2c1 - 18.19a2b2 - 1.55a2c2 + 2.55b1c1 + 22.97b1b2 \\ & +0.76b1c2 - 2.51b2c1 - 6.26b2c2 - 0.73c1c2 - 1.61a1^2 - 71.20b1^2 \\ & -1.80c1^2 + 0.96a2^2 - 92.72b2^2 + 0.17c2^2 \end{aligned} \tag{3}$$

The equations contain the relationship between structural variables and platform fundamental frequency, structural variables and sensitivity, which can be used as a reference for optimization. The relationships between the structural parameter variables and the objective functions are shown in Figs. 6–8.

An analysis of variance was performed on the objective functions of the approximate model. The results are given in Table 3. For all objective functions, $p > 0.0001$, $R^2 > 0.8$, the difference between adjusted R^2 and predicted R^2 is less than 0.2, and the adequate precision is greater than 4, all of which meet the requirements. Eqs. (1) to (3) can thus be used to optimize the models. The final optimal parameters obtained are given in Table 2.

The geometric model with the optimal structural parameters was subjected to FEA again, and its objective functions were recorded. Table 4 shows that the objective function values obtained using Eqs. (1) to (3) are similar to those obtained in the analysis. This

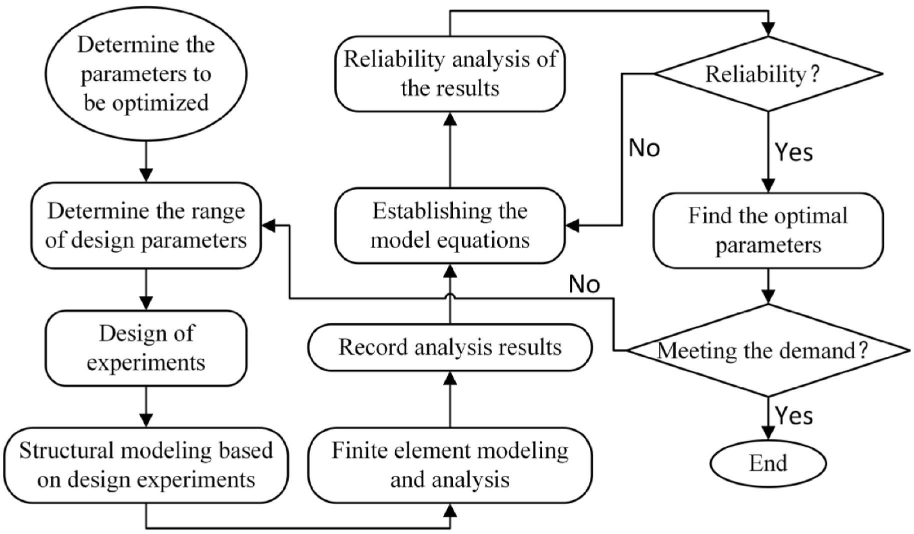

Fig. 5. Flowchart of structural parameter optimization.

Table 2
Parameter ranges for the elastic body.

Variable	a1	b1	c1	a2	b2	c2
Range(mm)	4 ~ 12	7 ~ 9	18 ~ 25	5 ~ 15	7 ~ 9	14 ~ 32
Optimal value(mm)	5	8.5	20.2	5	8.5	30

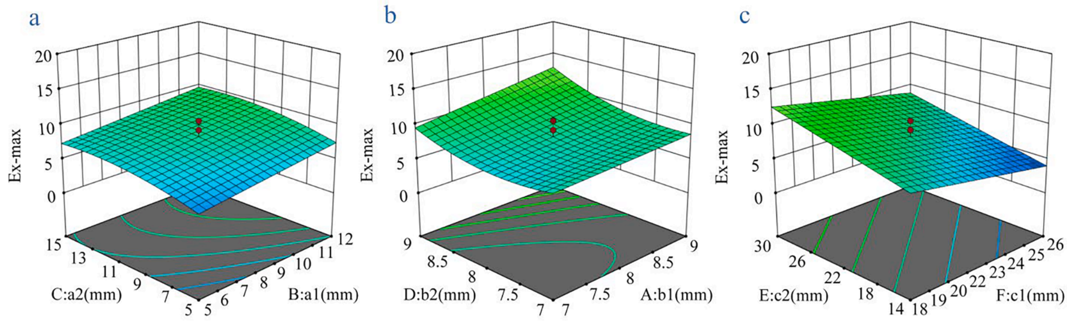

Fig. 6. Response surface for E_x-max vs structural parameter variables.

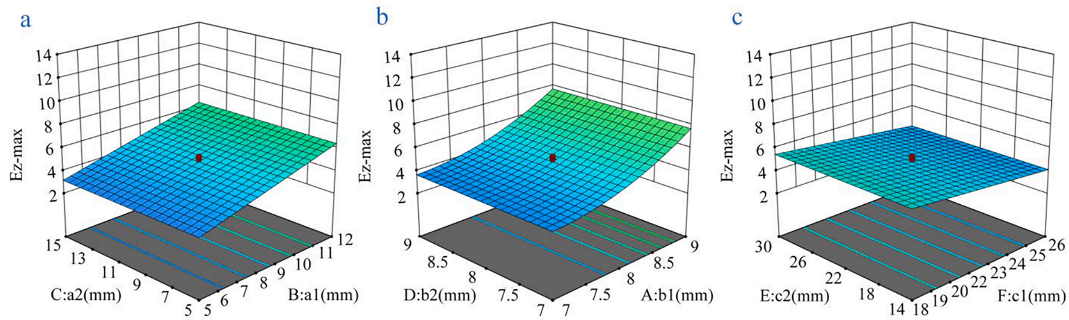

Fig. 7. Response surface for E_z-max vs structural parameter variables.

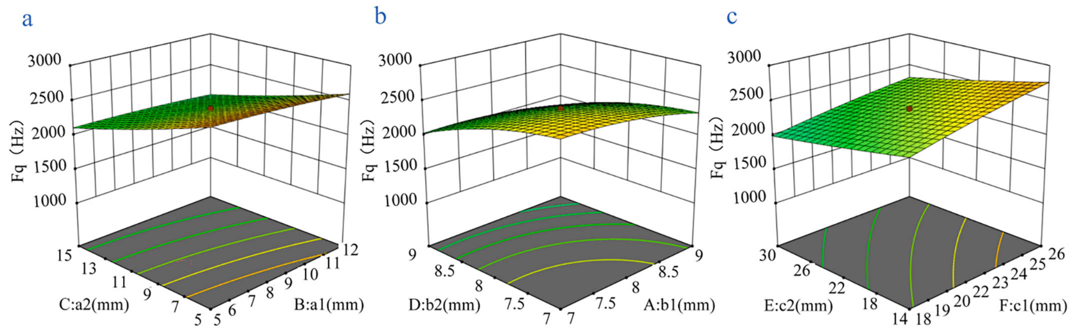

Fig. 8. Response surface for *Fq* vs structural parameter variables.

Table 3
Results of an analysis of variance.

Indicators	p values	R^2	Adjusted R^2	Predicted R^2	Adequate precision
E_x-max	<0.0001	0.89	0.86	0.81	24.85
E_z-max	<0.0001	0.82	0.81	0.79	21.36
Fq	<0.0001	0.99	0.98	0.95	40.44

similarity confirms that the optimized parameters can be used to manufacture the measurement platform.

The FEA of the entire measurement platform with optimal structural parameters was carried out (hex8 elements which have better computational accuracy were mainly used). A z-directional force of 1 N was applied to the measuring platform. Fig. 9 shows that the maximum stress in the platform under the force is 3.31×10^{-2} MPa. Knowing that the Young's modulus of the material $\boldsymbol{\sigma_s}$ is 460 MPa and setting the safety factor S to 1.2, the permissible maximum stress can be expressed as $\boldsymbol{\sigma_{Fs}} \le \boldsymbol{\sigma_s}/S = 383$ MPa. The load capacity of the platform is calculated as being greater than 1000 kg, which is sufficient for the requirements.

4. Measurement principle

The designed measurement platform is mainly used to measure the dynamic disturbance force, and its calculation principle is thus based on spectrum analysis, as the time domain signal contains little dynamic information. As previously mentioned, a strain monopodium is equivalent to a three-dimensional force sensor that can be used to measure $F_x(\omega)$, $F_y(\omega)$ and $F_z(\omega)$ and is known to have weak dimensional coupling through FEA. One strain monopodium subjected to a z-directional disturbance force is analyzed. Fig. 2 clearly shows that the magnitudes of deformation of R_1, R_2, R_3 and R_4 are the same (where R_1 and R_2 have the same direction of deformation and R_3 and R_4 have the same direction of deformation), and the distribution of the four strain gauges in the full bridge is shown in Fig. 10. The output voltage of the i-th strain monopodium subjected to a disturbance force in the z-direction is expressed as

$$Vout - iz(\omega) = \left(\frac{R4(\omega) + \Delta R4(\omega)}{R1(\omega) - \Delta R1(\omega) + R4(\omega) + \Delta R4(\omega)} - \frac{R3(\omega) - \Delta R3(\omega)}{R2(\omega) - \Delta R2(\omega) + R3(\omega) + \Delta R3(\omega)}\right) Vin - iz(\omega) \tag{4}$$

On the basis that $R_1(\omega) = R_2(\omega) = R_3(\omega) = R_4(\omega) = R(\omega)$ and $\Delta\ R_1(\omega) = \Delta\ R_2(\omega) = \Delta R_3(\omega) = \Delta\ R_4(\omega) = \Delta\ R(\omega)$, Eq. (4) can be rewritten as

$$\mathrm{Vout}\ \text{-}\ iz(\omega) = \frac{\Delta R(\omega)}{R(\omega)} \mathrm{Vin}\ \text{-}\ iz(\omega) \tag{5}$$

$V_{\text{out-}ix}(\omega)$ and $V_{\text{out-}iy}(\omega)$ are obtained in the same way. At this point, the three-dimensional disturbance force $\mathbf{F}_{\text{mono-}i}(\omega)$ acting on the i-th strained monopodium is calculated as

$$\boldsymbol{F}\mathrm{mono}\ \text{-}\ i(\omega) = \begin{bmatrix} Fix(\omega) \\ Fiy(\omega) \\ Fiz(\omega) \end{bmatrix} = \begin{bmatrix} ai1(\omega) & ai2(\omega) & ai3(\omega) \\ ai4(\omega) & ai5(\omega) & ai6(\omega) \\ ai7(\omega) & ai8(\omega) & ai9(\omega) \end{bmatrix} \begin{bmatrix} \mathrm{Vout}\ \text{-}\ ix(\omega) \\ \mathrm{Vout}\ \text{-}\ iy(\omega) \\ \mathrm{Vout}\ \text{-}\ iz(\omega) \end{bmatrix} i = 1, 2, 3, 4 \tag{6}$$

Eq. (6) is equivalent to

$$\boldsymbol{F}\mathrm{mono}\ \text{-}\ i(\omega) = \boldsymbol{A}i(\omega)\boldsymbol{V}i(\omega) \tag{7}$$

Therefore, 12 $F_{ix}(\omega)$, $F_{iy}(\omega)$ and $F_{iz}(\omega)$ are currently available for the four strain monopodia and can be used to calculate the six-dimensional disturbance force of the vibration source. In order to introduce as little systematic error as possible, suppose m of the 12 forces are selected and relabeled as $F_1(\omega)$,$F_2(\omega)$, …, $F_m(\omega)$ and the corresponding output voltages are denoted $V_1(\omega)$,$V_2(\omega)$, …, $V_m(\omega)$. The expression for the source disturbance force $\mathbf{F}(\omega)$ is obtained as

$$\boldsymbol{F}(\omega) = \begin{bmatrix} Fx(\omega) \\ Fy(\omega) \\ Fz(\omega) \\ Mx(\omega) \\ My(\omega) \\ Mz(\omega) \end{bmatrix} = \boldsymbol{B}(\omega) \begin{bmatrix} F1(\omega) \\ F2(\omega) \\ \vdots \\ Fm(\omega) \end{bmatrix} = \boldsymbol{D}(\omega) \begin{bmatrix} V1(\omega) \\ V2(\omega) \\ \vdots \\ Vm(\omega) \end{bmatrix} \tag{8}$$

where $\mathbf{B}(\omega)$ is the transformation matrix of the m output forces from the strain monopodia and the vibration source disturbance force. Equation (8) is equivalent to

$$\boldsymbol{F}(\omega) = \boldsymbol{D}(\omega)\boldsymbol{V}(\omega) \tag{9}$$

where $\mathbf{D}(\omega)$ is the $6 \times m$ coefficient matrix, and the source disturbance force $\mathbf{F}(\omega)$ can be calculated if $\mathbf{D}(\omega)$ can be determined.

The vibration source location, mass, moisture, temperature and environmental disturbances are uncertainties in each measurement, and thus to reduce the effects of these factors on the measurement accuracy, a calibration experiment is conducted before each measurement to determine which m output voltages should be selected from strain monopodia as $\mathbf{V}(\omega)$ and to re-obtain the matrix $\mathbf{D}$

Table 4
Comparison of simulated and predicted values of the objective function.

Objective function	E_x-max	E_z-max	Fq(Hz)
Predicted values	13.8	8.4	2168.13
Simulated values	13.9	8.1	2153.68
Relative error	0.72 %	3.57 %	0.67 %

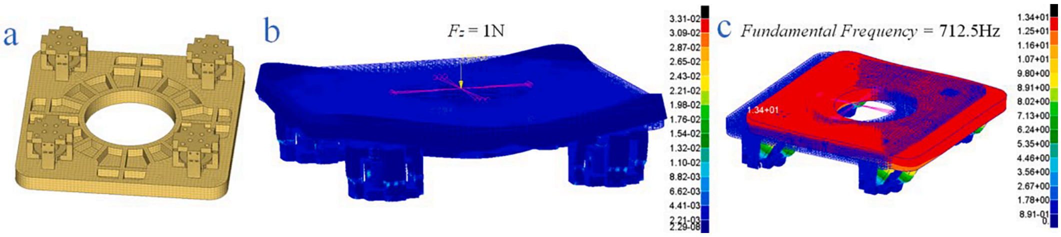

Fig. 9. FEA of the measurement platform: (a) FEM mesh; (b) stress under $F_z = 1$ N; (c) fundamental frequency.

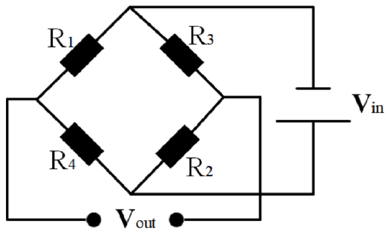

Fig. 10. Schematic of the full bridge circuit.

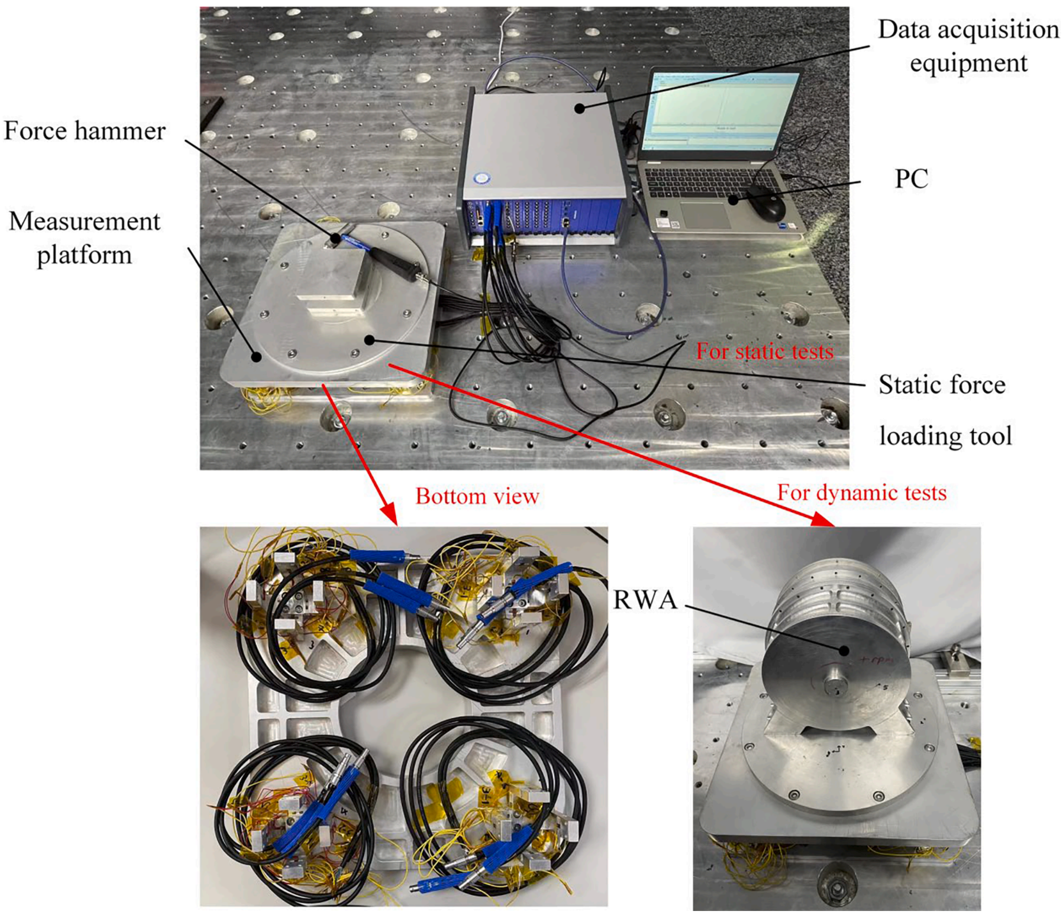

Fig. 11. Test system.

(ω).

In the calibration experiment, $\mathbf{F}_c(\omega)$ is the known disturbance force (where the subscript c indicates calibration), $\mathbf{V}_{c\text{-}cs}(\omega)$ denotes the 12 measured output voltages (called the candidate set), and m output voltages are selected from the candidate set to form $\mathbf{V}_c(\omega)$. We have the equation

$$\boldsymbol{V}c(\omega) = \boldsymbol{E}c(\omega)\boldsymbol{F}c(\omega) \tag{10}$$

The coefficient matrix is obtained using the pseudo-inverse matrix from Eq. (10):

$$\boldsymbol{E}c(\omega) = \boldsymbol{V}c(\omega)\boldsymbol{F}c^{\mathrm{T}}(\omega)[\boldsymbol{F}c(\omega)\boldsymbol{F}c^{\mathrm{T}}(\omega)]^{-1} \tag{11}$$

Substituting Eq. (11) into Eq. (10) yields the estimate of the disturbance force $\mathbf{F}_c'(\omega)$:

$$\boldsymbol{F}c^{'}(\omega) = [\boldsymbol{E}c^{\mathrm{T}}(\omega)\boldsymbol{E}c(\omega)]^{-1}\boldsymbol{E}c(\omega)\boldsymbol{V}c(\omega) \tag{12}$$

The accuracy of the estimated input disturbance force $\mathbf{F}_c'(\omega)$ depends on the selection of m output voltages from $\mathbf{V}_{c\text{-}cs}(\omega)$. We use D optimization [37–39] to select the optimal $\mathbf{V}_c(\omega)$.

Assuming that the errors in strain measurement are statistically independent and that their standard deviation is σ, the covariance matrix of $\mathbf{F}_c'(\omega)$ is $var[\mathbf{F}_c'(\omega)] = \sigma^2[\mathbf{E}_c^{\mathrm{T}}(\omega)\mathbf{E}_c(\omega)]^{-1}$, where σ^2 is a constant and $[\mathbf{E}_c^{\mathrm{T}}(\omega)\mathbf{E}_c(\omega)]^{-1}$ is the sensitivity of $\mathbf{F}_c'(\omega)$; lower sensitivity corresponds to higher accuracy of $\mathbf{F}_c'(\omega)$ [37]. Therefore, the most accurate $\mathbf{F}_c'(\omega)$ can be obtained by selecting the m output voltages that maximize the value of $|\mathbf{E}_c^{\mathrm{T}}(\omega)\mathbf{E}_c(\omega)|$ (which is called D optimal design, where D refers to the determinant), and the optimal output voltage $\mathbf{V}_c(\omega)$ can be found using the sequential exchange method [40]. The coefficient $\mathbf{D}(\omega)$ can be expressed as

$$\boldsymbol{D}(\omega) = [\boldsymbol{E}c^{\mathrm{T}}(\omega)\boldsymbol{E}c(\omega)]^{-1}\boldsymbol{E}c(\omega) \tag{13}$$

From the above calculation steps, we can obtain expression (9) used to solve for the disturbance force of the vibration source. The proposed measurement platform can also be used for static force measurements, with the measurement principles being the same as those described above.

5. Experiment

On the basis of the design and optimization mentioned above, a prototype of the measurement platform was manufactured. Strain gauges were affixed to the elastic bodies of the four strain monopodia (shown in Fig. 11). After the calibration test of the platform, the dynamic and static mechanical characteristics of the platform were investigated.

5.1. Platform parameter verification and calibration experiments

Fig. 11 shows a test system comprising a measurement platform, reaction wheel assembly (RWA), data acquisition equipment (precision: ±0.1 dB; 652u-24 bit, IOtech, Norton, MA, USA), static force loading tool, and force hammer (5800B5, PCB; sensitivity: 1.128 mV/N).

Firstly, the measurement of the platform's fundamental frequency was carried out. Without installing the RWA and the static force loading tool, the striking of a force hammer on the measurement platform provided a platform fundamental frequency of 749.5 Hz (as shown in Fig. 12, where the output of channel 1 was selected randomly and the output voltage from the channel can be calculated as a strain value) at a sampling frequency of 4096 Hz (to avoid aliasing and to improve computational efficiency, the sampling factor is 2.56 throughout the paper) whereas the simulation result is 712.5 Hz as shown in Fig. 9. The experimental results show that the dynamic

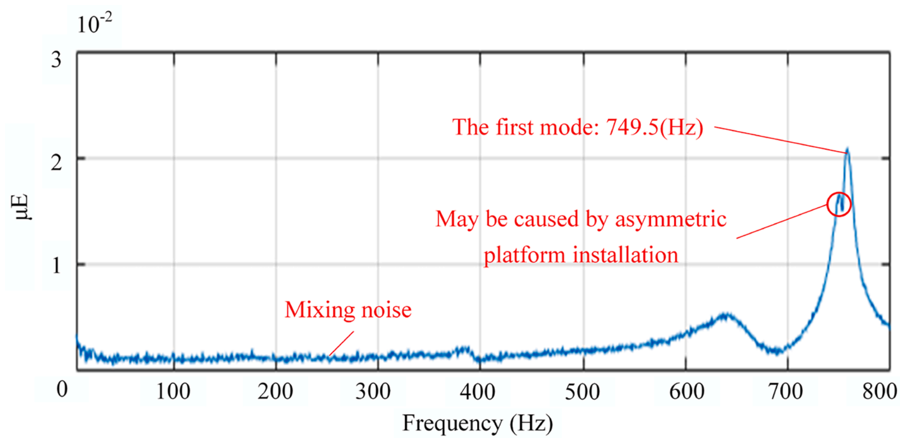

Fig. 12. Output of channel 1 (which introduces noise into the signal).

characteristics of the platform can be obtained accurately using the simulation model. A fundamental frequency of 749.5 Hz is adequate for meeting the requirements of the measurement range of 3–300 Hz for the optical facility, where the RWA was used as the vibration source of the optical facility.

The coordinates of points of the input forces were determined to obtain the subsequent matrix **C** prior to mounting the RWA for calibration experiments. The coordinates of the input force points on the RWA were measured with a portable measuring arm (Hexagon Absolute Arm 6-Axis, model 8725–6) as shown in Fig. 13-a, with the coordinates originating from the center of the upper plane of the RWA base. The RWA coordinate system and the locations of the calibration points are shown in Fig. 13b and c. The coordinates of the six input points are given in Table 5.

After that, the calibration is ready to start. The RWA was then mounted on the measurement platform (shown in Fig. 11, dynamic tests). The force hammer was used to input the impact signals via the measured calibration points and the data acquisition equipment was used to obtain the 12 output signals. The dynamic calibration matrix **D**(ω) in Eq. (9) can be obtained with this system. In the dynamic calibration experiments, the force hammer was used to hammer at six calibration points sequentially. Each point was hammered three times and the data from the hammer and output channels were then averaged as $\mathbf{F}_c(\omega)$ and $\mathbf{V}_c(\omega)$ to reduce the effect of random errors. Note that the input forces here need to be converted to the forces and moments acting at the center of the upper plane of the RWA base in the time domain using Eq. (14), where **C** is given by Eq. (15) and $F_{\text{in-}i}$ is the input force acting at point *i*. Using six output signals for the calculation (i.e., $m = 6$, to introduce less systematic errors and avoid ill-conditioning matrices), the calibration matrix **D**(ω) can be determined as expressed in Eq. (16) adopting Eqs. (10)–(13) and D optimal design. Which six channels are optimal can also be determined. When adopting a data sampling frequency of 1024 Hz (because the frequency band of interest for the RWA is in the range of 3–300 Hz) and a sampling time of 8 s, each element of the calibration matrix $\mathbf{D}_{ij}(\omega)$ has a length of 8192 and an effective bandwidth of 1/12.8–400 Hz. The equations are

$$\boldsymbol{F}c(t) = \boldsymbol{C}\begin{bmatrix} Fin-1(t) & 0 & 0 & 0 & 0 & 0 \\ 0 & Fin-2(t) & 0 & 0 & 0 & 0 \\ 0 & 0 & Fin-3(t) & 0 & 0 & 0 \\ 0 & 0 & 0 & Fin-4(t) & 0 & 0 \\ 0 & 0 & 0 & 0 & Fin-5(t) & 0 \\ 0 & 0 & 0 & 0 & 0 & Fin-6(t) \end{bmatrix} \tag{14}$$

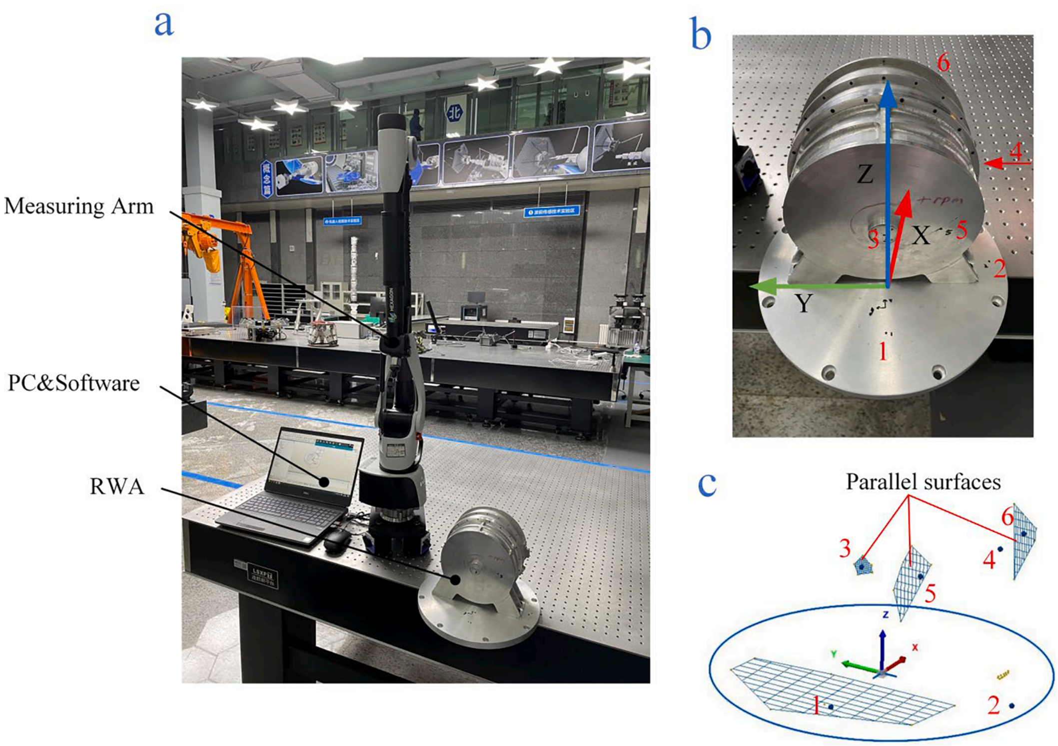

Fig. 13. Measurement of input force points: (a) measuring equipment; (b) coordinate system and input force points for the RWA; (c) positions of the input force points on the RWA in the software.

Table 5
Coordinates of the calibration force input points.

	Position (mm)					
Direction	Point 1	Point 2	Point 3	Point 4	Point 5	Point 6
X-axis	−89.581	0.809	−38.842	32.090	−30.724	102.5
Y-axis	−1.959	−131.544	0.372	97.794	−54.559	−80.017
Z-axis	0.000	0.000	113.988	129.263	115.309	114.287

$$\boldsymbol{C} = \begin{bmatrix} 0 & 0 & 1 & 0 & 1 & -1 \\ 0 & 0 & 0 & 1 & 0 & 0 \\ -1 & -1 & 0 & 0 & 0 & 0 \\ 0.001959 & 0.131544 & 0 & -0.129263 & 0 & 0 \\ -0.089581 & 0.000809 & 0.113988 & 0 & 0.115309 & -0.114287 \\ 0 & 0 & -0.000372 & 0.032090 & 0.054559 & -0.080017 \end{bmatrix} \tag{15}$$

$$\boldsymbol{D}_{6\times6}(\omega) = \begin{bmatrix} \boldsymbol{D}_{11}(\omega) & \cdots & \boldsymbol{D}_{16}(\omega) \\ \vdots & \ddots & \vdots \\ \boldsymbol{D}_{61}(\omega) & \cdots & \boldsymbol{D}_{66}(\omega) \end{bmatrix} \tag{16}$$

5.2. Dynamic mechanical performance test

The forces to be measured at optical facilities range in magnitude from a few Newtons to several hundred Newtons, and good linearity is thus fundamental to the platform. We verified dynamic linearity by conducting a calibration experiment. Using a hammer, impulses of different amplitudes were input to the RWA to obtain a transfer function between calibration point 1 and output channel 2 (Fig. 14). Using an input force of 54.1 N as a reference, the relative errors for input pulses of 26.4 and 96.7 N are presented in Table 6, showing an average relative error of 4.28 %. This approach is intended to describe the linearity of individual output over a wide frequency band and does not adequately reflect the dynamic linearity of the six-dimensional output of the platform after dynamic calibration.

The precision of the platform was then tested by measuring the impact signal in the frequency domain. By applying a force to the RWA with a force hammer, the input force was calculated by substituting the data of the six optimal channels from D optimization into Eq. (9). A plot of the actual input (F_x) versus the measured force is shown in Fig. 15. The dynamic relative error of the platform can be calculated to be within 3 %. The figure shows that the strain measuring platform has good low-frequency measurement capability. In addition, the calculation of an arbitrary selection of 6 channels without D optimization gives a red curve as shown in Fig. 15, which shows that D optimization has selected the channels with better signal quality and improved measurement accuracy.

In addition, the actual in-orbit vibration source disturbance was simulated through a six-dimensional disturbance simulator [41] to further examine the precision of the platform under multi-frequency sinusoidal excitation, especially in the low frequency band (re-calibration has been carried out before the measurement). The test system is shown in Fig. 16. The simulator was fitted with a load that allows the simulator to provide higher accuracy in low frequency vibration. In the Fig. 17, the disturbance outputs (F_x, M_y) of the in-

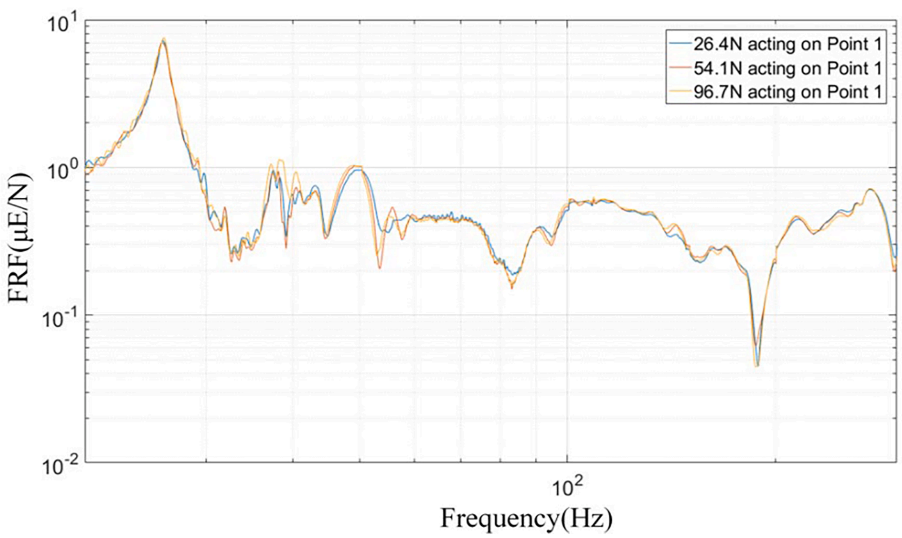

Fig. 14. Transfer function (with the RWA) for different amplitude impulses.

Table 6
Relative error of the transfer function for different amplitude impulses.

Frequency range (Hz)	Relative error (%)	
	26.4 N	96.7 N
3–50	3.46	2.91
50–100	6.98	5.16
100–150	3.59	2.27
150–200	6.36	7.05
200–250	1.55	4.16
250–300	6.35	1.56

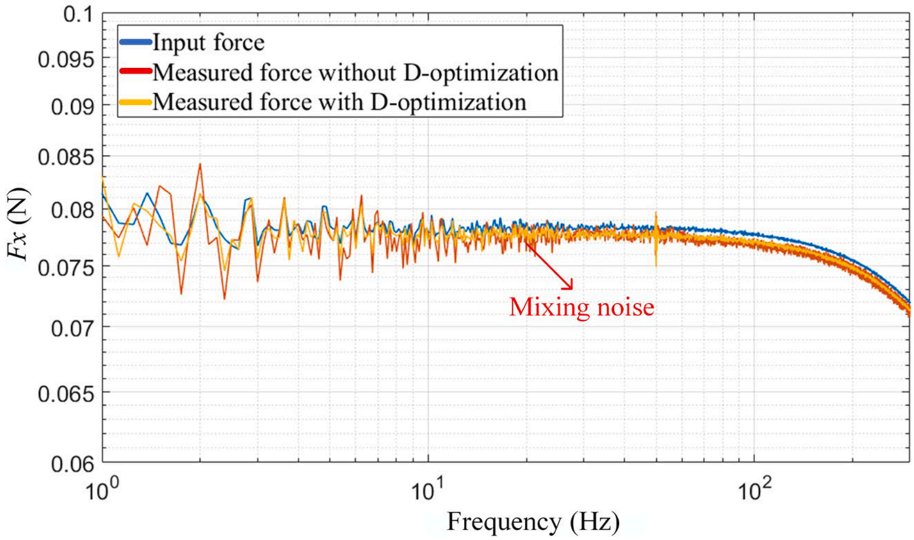

Fig. 15. Comparison of the impact input force (F_x) with the measured force.

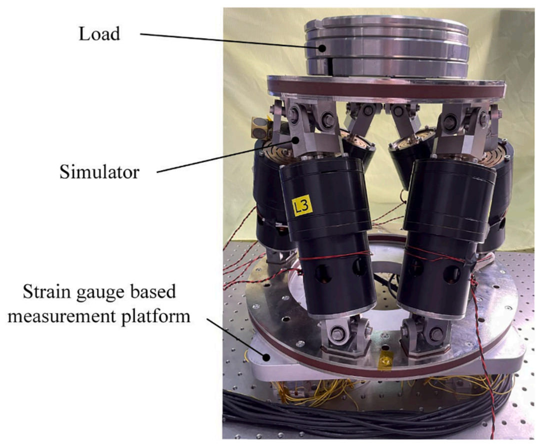

Fig. 16. Test system with simulator.

orbit CMG and cryocooler were simulated, where 46.7 Hz was the CMG disturbance frequency, 80 Hz was the cryocooler disturbance frequency, and the 8 Hz excitation was to detect the low frequency characteristics of the system. The data in the Fig. 17 shows that the dynamic measurement accuracy of the platform is within 5.6 %, which is good even at low frequencies.

We next tested the vibration of the RWA at different speeds as a practical application of the platform. A measuring platform described in the literature [4] (having dynamic relative error less than 5 %) was used for comparison. Fig. 18 shows that the piezoelectric measuring platform measures disturbance forces of the RWA. The RWA was controlled using an STM 32 with a proportional–integral–derivative algorithm to change its speed. The RWA was spun at rates ranging between 60 and 2940 revolutions per

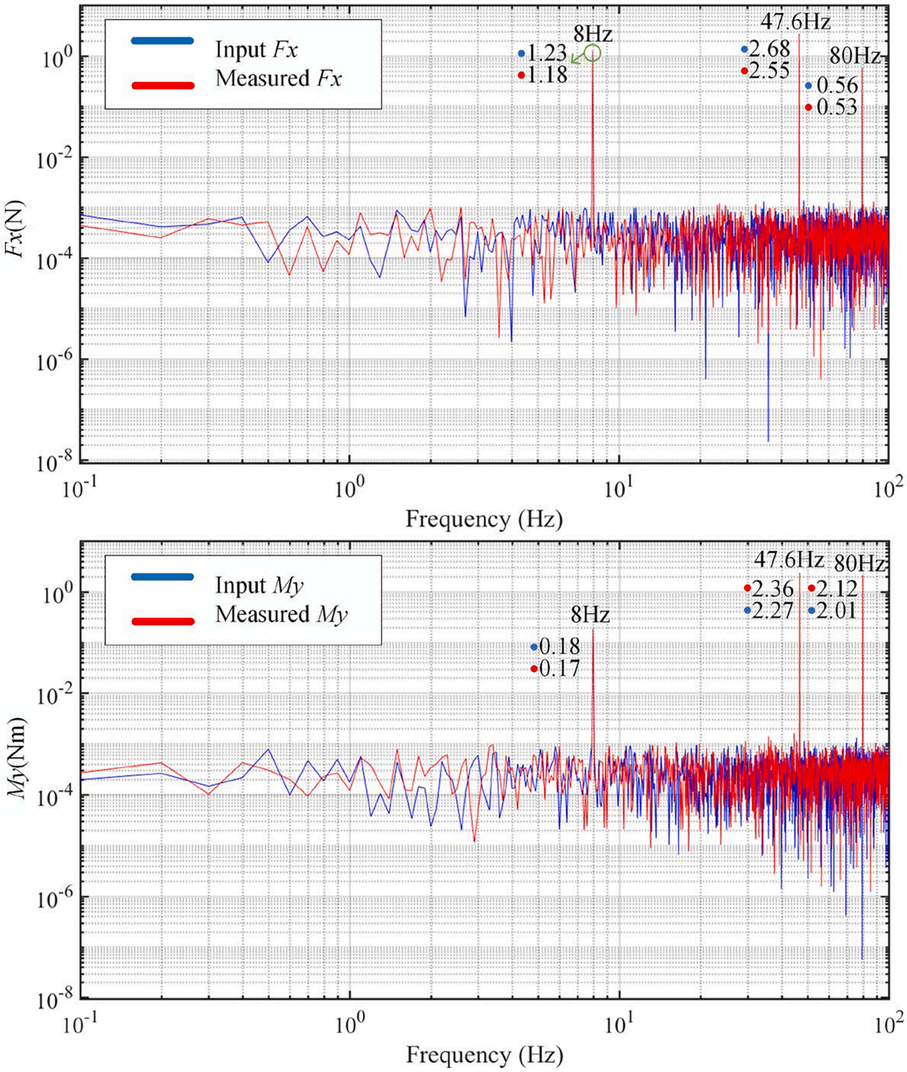

Fig. 17. Comparison of the input force generated by the simulator with the measured force by strain gauges platform.

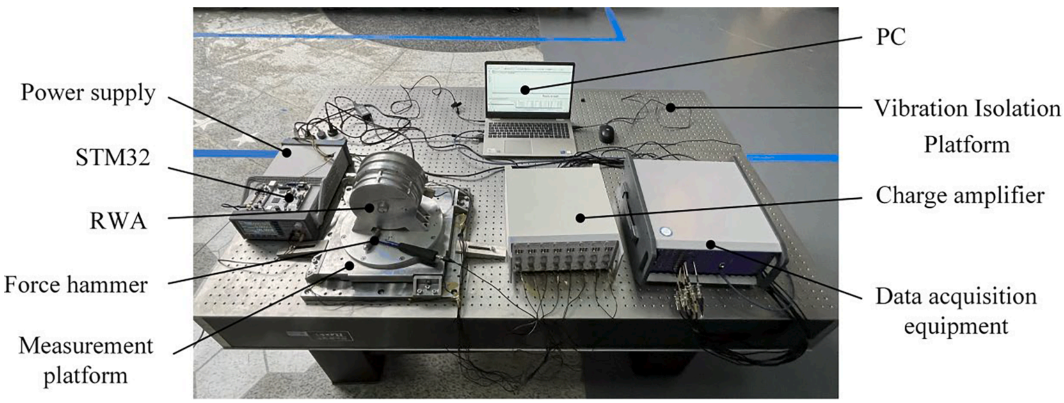

Fig. 18. Piezoelectric measuring platform for measuring disturbance forces of the RWA.

minute (RPM) in increments of 60 RPM, and disturbances were measured for each speed at a sampling rate of 1024 Hz for 8 s. Similarly, measurements were made of the RWA disturbance force using a strain-gauge-based measuring platform. A waterfall plot of the RWA x-direction force and y-direction moment measured using the strain measuring platform is shown in Fig. 19. The figure shows the rocking mode of the RWA, which represents both forward and reverse processions and forms a V-shaped curve. Additionally, the structural mode curve in Fig. 19 does not change with variations in the rotor speed and is mainly related to the elasticity of the structure. Fig. 20 compares the x-direction disturbance forces measured by the piezoelectric and strain platforms at speed of 1980 RPM. It can be seen that the vibration curves obtained using the strain platform and piezoelectric platform coincide well in high frequency band, but piezoelectric platform has poor low frequency measurement accuracy.

Fig. 20 also compares the disturbance forces obtained with and without D optimization using the strain-gauge-based platform. The vibration curves obtained with D optimization are clearly of higher quality, which demonstrates the effectiveness of D optimization. It is assumed that D optimization selects the optimal output channels that are less disturbed by noise and improves the measurement accuracy.

5.3. Static mechanical performance test

The static mechanical characteristics of the platform were tested and experiments were carried out to investigate the linearity, repeatability and relative error. A schematic of the test system and photograph of the measurement equipment are shown in Fig. 21. The principle of the static force test was exactly the same as that of the dynamic force test. The limits of the force and moment in this test were 500 N and 300 Nm, respectively. The output without a load was recorded before the measurement experiment and subtracted from the measurement results.

Photograph of the measurement equipment.

In the test, a force sensor (208C03, PCB; sensitivity: 2.248 mV/N; resolution: 0.02 *N*-rms; range: 2.224 kN) was used to detect the

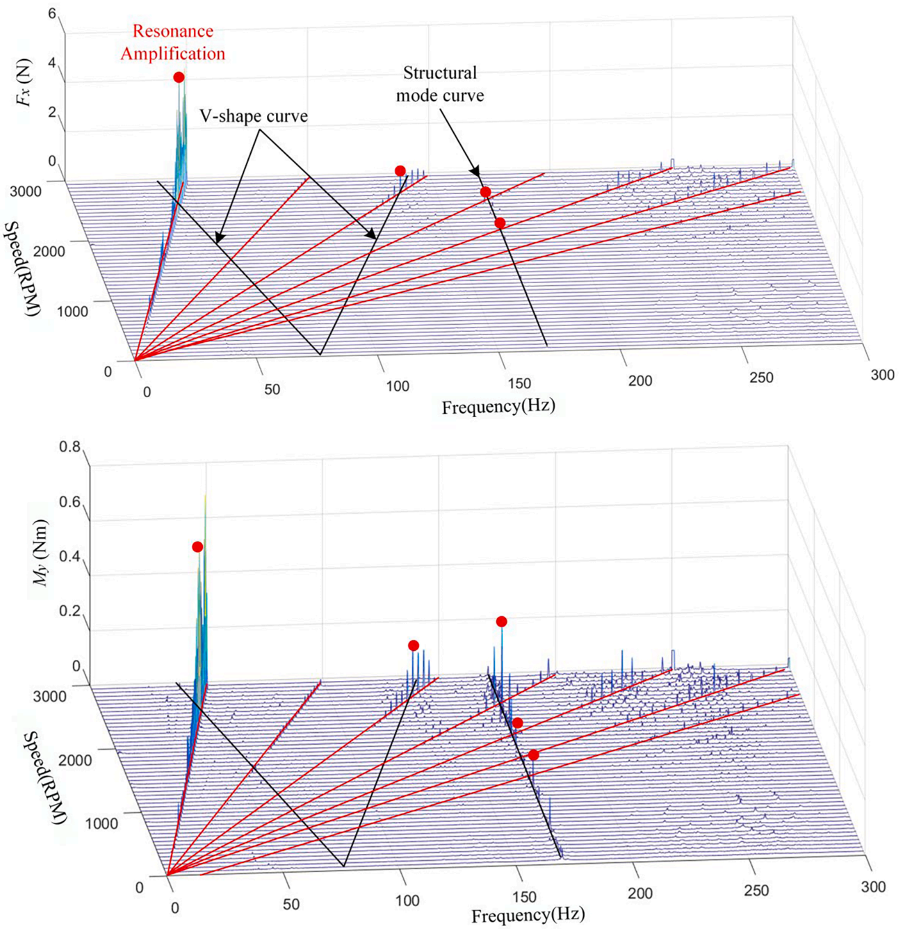

Fig. 19. Waterfall diagram of the RWA disturbance force measured using the strain-gauge-based platform: (a) F_x; (b) M_y.

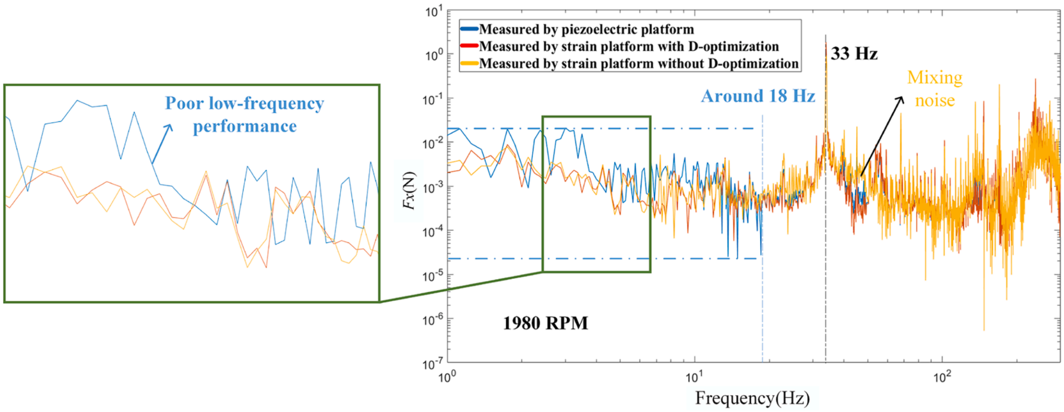

Fig. 20. Disturbance forces F_x measured at 1980 RPM.

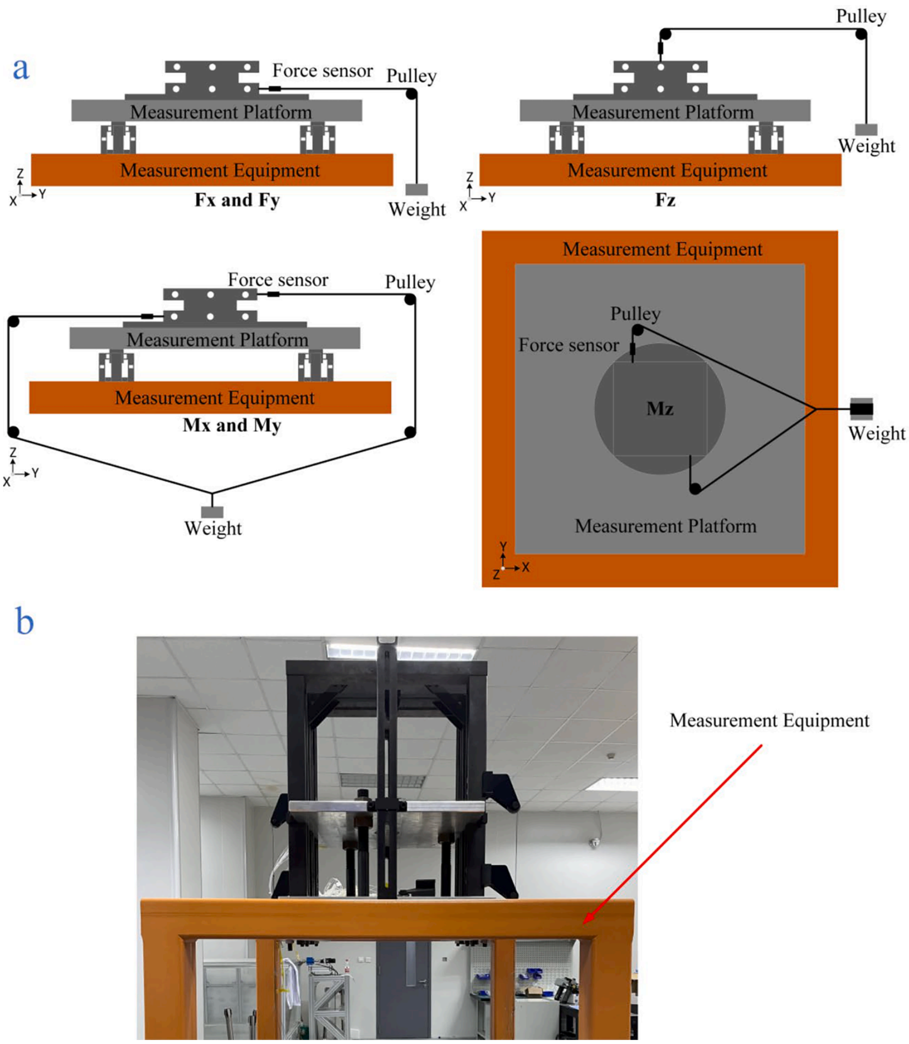

Fig. 21. Static mechanical performance test system: (a) schematic diagram of the system;

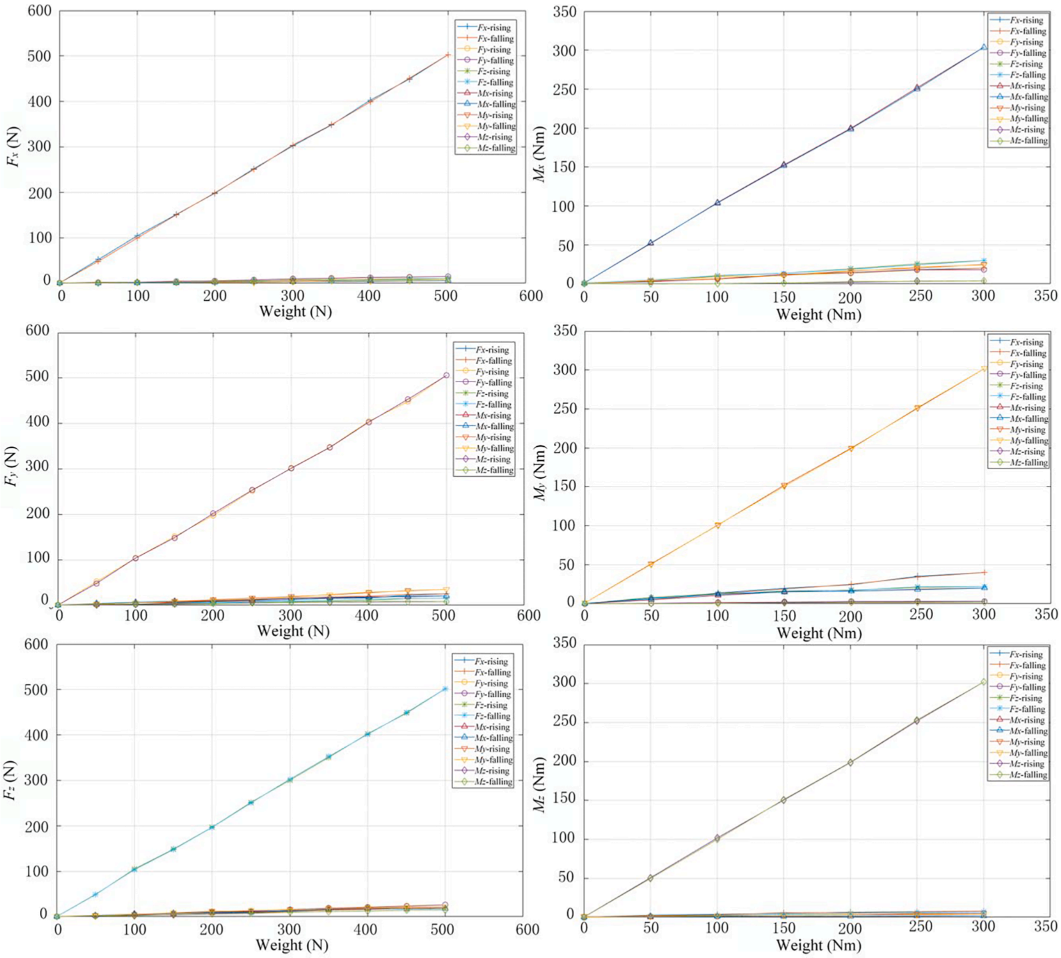

Fig. 22. Static input force vs measured force.

Table 7
Statistical data on static mechanical properties.

Force/Moment (N; Nm)	Nonlinearity (%FS)	Repeatability error (%FS)	Static relative error (%FS)
F_x	0.82	0.96	2.14
F_y	1.20	1.01	3.31
F_z	1.03	0.44	2.07
M_x	1.42	0.61	1.83
M_y	0.81	0.53	0.96
M_z	1.13	0.62	1.24

magnitude of the loading force and the weights (5 kg; precision: $\pm$1%) were loaded one by one. The loading and unloading process was repeated three times. The input and measured forces are shown in Fig. 22. Table 7 statistically presents the static characteristics parameters, showing that the linearity of the platform is within 1.5 %FS, the repeatability is within 1.1 %FS and the static relative error is within 5 %FS.

6. Conclusions

This paper described the design, optimization, analysis and testing of a quadrupedal dynamic disturbance force measurement platform that can be used to measure the disturbance force of low-frequency sources in large optical facilities. The use of four strain monopodia improves the rigidity of the platform. Response surface methodology is adopted to balance the sensitivity and stiffness of the platform, whereas the precision is improved through D optimization. Simulation and experimental results show that the load capacity of the platform is greater than 1000 kg and the dynamic relative error in the frequency range of 3–300 Hz is less than 5.6 %, whereas the peak value remains near 10 %. The static relative error of the platform is within 5 %, the linearity of the platform is within

1.5 %FS, and the repeatability is within 1.1 %FS. The platform has good performance in terms of its low-frequency dynamic characteristics, stiffness and accuracy. The analysis and optimization methods adopted in this paper can be applied to measurement platforms of other size and type.

Funding

This work was supported by the National Natural Science Foundation of China (NO. 11672290).

Declaration of Competing Interest

The authors declare that they have no known competing financial interests or personal relationships that could have appeared to influence the work reported in this paper.

Data availability

The authors do not have permission to share data.

References

[1] Y. Sun, D.S. Deng, H.B. Yuan, Precision of the chinese space station telescope (CSST) stellar radial velocities, Res. Astron. Astrophys. 21 (4) (2021) 092, https://doi.org/10.1088/1674-4527/21/4/92.
[2] Y.e. Cao, Y. Gong, Z.-Y. Zheng, C. Xu, Calibrating photometric redshift measurements with the multi-channel imager (MCI) of the china space station telescope (CSST), Res. Astron. Astrophys. 22 (2) (2022) 025019.
[3] F. Arranz Martínez, R. Martín Ferrer, G. Palacios-Navarro, et al., Study on the vibration characteristics of the telescope T80 in the javalambre astrophysical observatory (JAO) aimed at Detecting Invalid Images, Sensors 20 (22) (2020) 6523, https://doi.org/10.3390/s20226523.
[4] M.Y. Xia, Z.B. Xu, K. Han, Q. Huo, A. Li, Dynamic disturbance force measurement platform for large moving device in spacecraft, J. Sound Vib. 447 (2019) 61–77, https://doi.org/10.1016/j.jsv.2019.01.053.
[5] L. Li, L. Tan, L. Kong, D. Wang, H. Yang, The influence of flywheel micro vibration on space camera and vibration suppression, Mech. Syst. Sig. Process. 100 (2018) 360–370.
[6] Y.J. Li, J. Zhang, Z.Y. Jia, et al., Research on a novel parallel spoke piezoelectric 6-DOF heavy force/torque sensor, Mech. Syst. Sig. Process. 36 (1) (2013) 152–167, https://doi.org/10.1016/j.ymssp.2012.03.016.
[7] R. Liang, Q.M. Wang, High sensitivity piezoelectric sensors using flexible PZT thick-film for shock tube pressure testing, Sens. Actuat. A 235 (2015) 317–327, https://doi.org/10.1016/j. sna.2015.09.027.
[8] Y. Sujana, G. Uma, M. Umapathy, Design and testing of piezoelectric resonant pressure sensor, Sens. Actuat. A 250 (2016) 177–186, https://doi.org/10.1016/j.sna.2016.09.031.
[9] Y.J. Li, et al., Research on the parallel load sharing principle of a novel self-decoupled piezoelectric six-dimensional force sensor, ISA Trans. 70 (2017) 447–457, https://doi.org/10.1016/j. isatra.2017.07.008.
[10] X. Cheng, Y.i. Gong, Y. Liu, Z. Wu, X. Hu, Flexible tactile sensors for dynamic triaxial force measurement based on piezoelectric elastomer, Smart Mater. Struct. 29 (7) (2020) 075007.
[11] K. Kim, J. Kim, X. Jiang, T. Kim, M. Gasulla, Static force measurement using piezoelectric sensors, J.Sens. 2021 (2021) 1–8.
[12] L.P. Chao, L.T. Chen, Shape optimal design and force sensitivity evaluation of six-axis force sensors, Sens. Actuat.A 63 (2) (1997) 105–112, https://doi.org/10.1016/S0924-4247 (97)01534-3.
[13] S.A. Liu, H.L. Tzo, A novel six-component force sensor of good measurement isotropy and sensitivities, Sens. Actuat.A 100 (2-3) (2002) 223–230, https://doi.org/10.1016/S0924-4247(02)00135-8.
[14] J.J. Park, G.S. Kim, Development of the 6-axis force/moment sensor for an intelligent robot's grippe, Sens. Actuat. A 118 (1) (2005) 127–134, https://doi.org/10.1016/j.sna. 2004.07.013.
[15] G.-S. Kim, Design of a six-axis wrist force/moment sensor using FEM and its fabrication for an intelligent robot, Sens. Actuat. A 133 (1) (2007) 27–34, https://doi.org/10.1016/j.sna.2006.03.038.
[16] C. Jacq, B. Lüthi, T.h. Maeder, O. Lambercy, R. Gassert, P. Ryser, Thick-film multi-DOF force/torque sensor for wrist rehabilitation, Sens. Actuat. A 162 (2) (2010) 361–366.
[17] Q. Liang, D. Zhang, Q. Song, Y. Ge, H. Cao, Y.u. Ge, Design and fabrication of a six-dimensional wrist force/torque sensor based on E-type membranes compared to cross beams, Measurement 43 (10) (2010) 1702–1719.
[18] B. Wu, J. Luo, F. Shen, et al., Optimum design method of multi-axis force sensor integrated in humanoid robot foot system, Measurement 44 (9) (2011) 1651–1660, https://doi.org/10.1016/j. measurement.2011.06.013.
[19] J.Q. Ma, A.G. Song, Fast estimation of strains for cross-beams six-axis force/torque sensors by mechanical modeling, Sensors 13 (5) (2013) 6669–6686, https://doi.org/10.3390/s130506669.
[20] Y. Sun, Y. Liu, T. Zou, M. Jin, H. Liu, Design and optimization of a novel six-axis force/torque sensor for space robot, Measurement 65 (2015) 135–148.
[21] E. DiGiampaolo, A. DiCarlofelice, A. Gregori, An RFID-enabled wireless strain gauge sensor for static and dynamic structural monitoring, IEEE Sens. J. 17 (2) (2016) 286–294, https://doi.org/10.1109/jsen.2016.2631259.
[22] K. Han, L. Chen, M. Xia, Q. Wu, Z. Xu, G. Wang, Design and optimization of a high sensitivity joint torque sensor for robot fingers, Measurement 152 (2020) 107328.
[23] A.G. Leal-Junior, et al., Polymer optical fiber strain gauge for human-robot interaction forces assessment on an active knee orthosis, Opt. Fiber Technol. 41 (2018) 205–211, https://doi.org/10.3390/s19143156.
[24] A. Leal-Junior, A. Frizera, H. Lee, Y. Mizuno, K. Nakamura, T. Paixão, C. Leitão, M.F. Domingues, N. Alberto, P. Antunes, P. André, C. Marques, M.J. Pontes, Strain, temperature, moisture, and transverse force sensing using fused polymer optical fibers, Opt. Express 26 (10) (2018) 12939.
[25] Urda, Pedro, et al. Wheel-rail contact force measurement using strain gauges and distance lasers on a scaled railway vehicle. Mechanical Systems and Signal Processing 138 (2020): 106555. https://doi.org/10.1016/j.ymssp.2019. 106555.
[26] A. Warsewa, M. Böhm, F. Guerra, J.L. Wagner, T. Haist, C. Tarín, O. Sawodny, Self-tuning state estimation for adaptive truss structures using strain gauges and camera-based position measurements, Mech. Syst. Sig. Process. 143 (2020) 106822.
[27] C.J. Li, A. Galip Ulsoy, High-precision measurement of tool-tip displacement using strain gauges in precision flexible line boring, Mech. Syst. Sig. Process. 13 (4) (1999) 531–546, https://doi.org/10.1006/mssp.1999.1223.
[28] T.A. Dwarakanath, B. Dasgupta, T.S. Mruthyunjaya, Design and development of a Stewart platform based force–torque sensor, Mechatronics 11 (7) (2001) 793–809, https://doi.org/10.1016/S0957-4158(00)00048-9.

[29] Y.L. Hou, et al., Optimal design of a hyperstatic Stewart platform-based force/torque sensor with genetic algorithms, Mechatronics 19 (2) (2009) 199–204, https://doi.org/10.1016/j.mechatronics.2008.08. 002.
[30] Z.Y. Jia, S. Lin, W. Liu, Measurement method of six-axis load sharing based on the Stewart platform, Measurement 43 (3) (2010) 329–335, https://doi.org/10.1016/j.measurement.2009.11.005.
[31] Y.-J. Li, B.-Y. Sun, J. Zhang, M. Qian, Z.-Y. Jia, A novel parallel piezoelectric six-axis heavy force/torque sensor, Measurement 42 (5) (2009) 730–736.
[32] Y.-J. Li, J. Zhang, Z.-Y. Jia, M. Qian, A novel piezoelectric 6-component heavy force/moment sensor for huge heavy-load manipulator's gripper, Mech. Syst. Sig. Process. 23 (5) (2009) 1644–1651.
[33] Khuri, et al., Response surface methodology, Wiley Interdiscip. Rev. Comput. Stat. 2 (2) (2010) 128–149, https://doi.org/10.1002/wics.73.
[34] G.E.P. Box and K.B. Wilson. On the experimental attainment of optimum conditions. Breakthroughs in statistics. Springer, New York, NY, 1992. 270-310. https://doi.org/10.1007/978-1- 4612 -4380-9_23.
[35] T.A. Reddy. Applied Data Analysis and Modeling for Energy Engineers and Scientists. Springer, 2011.
[36] S.L.C. Ferreira, R.E. Bruns, H.S. Ferreira, G.D. Matos, J.M. David, G.C. Brandão, E.G.P. da Silva, L.A. Portugal, P.S. dos Reis, A.S. Souza, W.N.L. dos Santos, Box-Behnken design: An alternative for the optimization of analytical methods, Anal. Chim. Acta 597 (2) (2007) 179–186.
[37] D.K. Gupta, A.K. Dhingra, Input load identification from optimally placed strain gages using D-optimal design and model reduction, Mech. Syst. Sig. Process. 40 (2) (2013) 556–570, https://doi.org/10.1016/j.ymssp.2013.06.011.
[38] D.K. Gupta, A.K. Dhingra, A reduced modal parameter based algorithm to estimate excitation forces from optimally placed accelerometers, Inverse Prob. Sci. Eng. 25 (3) (2017) 397–417, https://doi.org/10.1080/17415977.2016.1169276.
[39] D.K. Gupta, A.K. Dhingra, Dynamic programming approach to load estimation using optimal sensor placement and model reduction, Int. J. Comput. Methods 15 (08) (2018) 1850071.
[40] Z. Galil, J. Kiefer. Time- and space-saving computer methods, related to Mitchell's DETMAX, for finding D-Optimum designs. Technometrics 22 (1980) 301-313. https://doi.org/10.1080 /00401706 .1980.10486161.
[41] X. Wang, Z. Xu, M. Xia, S. He, H. Li, Q. Wu, Research on a six-degree-of-freedom disturbance force and moment simulator for space micro-vibration experiments, J. Sound Vibr. 432 (2018) 530–548.